


## Article

# Characterization of Self-Powered Triboelectric Tachometer with Low Friction Force

Ling Bu \* , Xinbao Hou, Lanxing Qin, Zhiwei Wang, Feng Zhang, Feng Li and Tao Liu

School of Information Engineering, China University of Geosciences, Beijing 100083, China; 2004190005@cugb.edu.cn (X.H.); qlx0503@163.com (L.Q.); 1004182214@cugb.edu.cn (Z.W.); zffeng7975@cugb.edu.cn (F.Z.); 2104200005@cugb.edu.cn (F.L.); 1004182222@cugb.edu.cn (T.L.)

\* Correspondence: lingbu@cugb.edu.cn

**Abstract:** Self-powered triboelectric tachometers have wide application prospects in mechanical and electrical industries. However, traditional disc-type tachometers typically require large contact force, which burdens rotary load and increases frictional wear. To reduce the friction force of triboelectric tachometers, we present an alternative structure defined by flapping between rigid and flexible triboelectric layers. In this work, we further characterize this type of tachometer, with particular focus on the oscillating relationship between output voltage and rotation speed due to the plucking mechanism. This oscillating relationship has been demonstrated both theoretically and experimentally. For future self-powered triboelectric tachometers, the proved oscillating relationship can be applied as calibration criteria for further enhancing sensitivity and linearity in rotation measurement.

**Keywords:** self-powered; triboelectric; tachometer; low friction force



**Citation:** Bu, L.; Hou, X.; Qin, L.; Wang, Z.; Zhang, F.; Li, F.; Liu, T. Characterization of Self-Powered Triboelectric Tachometer with Low Friction Force. *Micromachines* **2021**, *12*, 1457. <https://doi.org/10.3390/mi12121457>

Academic Editors: Haixia (Alice) Zhang and Wei Tang

Received: 14 October 2021  
Accepted: 23 November 2021  
Published: 27 November 2021

**Publisher's Note:** MDPI stays neutral with regard to jurisdictional claims in published maps and institutional affiliations.



**Copyright:** © 2021 by the authors. Licensee MDPI, Basel, Switzerland. This article is an open access article distributed under the terms and conditions of the Creative Commons Attribution (CC BY) license (<https://creativecommons.org/licenses/by/4.0/>).

## 1. Introduction

In the Internet of Things era, massive sensing equipment is indispensable for the realization of intelligent buildings, transportation, cities, etc. [1]. Accompanying the large quantity of sensors in versatile environments is the equally massive demand of distributed and long-lasting power sources, which can hardly be satisfied by traditional powering methods like batteries or cables. Toward this demand, triboelectric nanogenerators present a promising power solution, as they can convert ambient tribology-related energy to electricity with quite high voltage, power, and efficiency [2–5]. Moreover, triboelectric nanogenerators can be inherently incorporated into sensors to construct self-powered devices [6–8], which further alleviates the powering issue and has already found numerous applications in wearable electronics [9–11], blue energy [12–14], infrastructure monitoring [15–17], etc.

Tachometers are widely needed in mechanical and electrical industries to characterize or monitor the rotation speed of shafts, gears, motors, etc. [18]. Constructing a self-powered tachometer is of huge industrial application interest. So far, there have been plenty of disc-based tachometers reported [19–23], which typically consist of a rotating disc with constant rotation speed and a fixed disc facing the rotating one. Because of the tight contact and large contact area, the friction force between the two discs is very high, and the triboelectric output is usually of high sensitivity. However, the large friction force also adds up to the load of the rotating disc, causing potential systematic errors in rotation speed characterization and increasing frictional wear of the measuring system in long-term monitoring [24,25]. Further, for most industrial applications, the revolving parts prefer measurement with less or even no contact, which renders it difficult to directly apply a disc-type tachometer to certain established industrial scenarios.

To reduce the frictional force of the triboelectric tachometer, Wang et al. designed a rotating sensor with polymer films connected to the shaft, sweeping and sliding through adjacent electrodes [26]. This design achieves ultra-low friction force, but the output

performance is limited compared with the simultaneously incorporated electromagnetic part. Zhang et al. proposed a non-contact cylindrical rotating triboelectric nanogenerator, but it required charge injection pre-treatment of the materials to guarantee output, and is actually based on the electrostatic induction principle [27]. Wu et al. applied the low frictional force triboelectric tachometer to the turbodrills with a structure similar to [26], but tested nonlinear voltage versus rotation speed relations [28]. Lin et al. rationally designed the rotation triboelectric nanogenerators to extend lifetime and durability by combining the rotating shaft with a spring, so that the contact force between the two rotating discs can be adjusted to a proper value through spring restoring force [29]. Previously, we have presented an alternative structure of a rotary triboelectric nanogenerator based on flapping between rigid and flexible triboelectric layers [30], which is based on the plucking mechanism, as a by-standing flexible blade is periodically perturbed by a rigid blade secured to the rotating parts. Because of the large deformation capability of the flexible blade, both contact force and friction force are significantly reduced, and tachometers based on this structure can be more readily applied in industrial scenarios. However, the output of this type of tachometers still suffers from the problem of accuracy and linearity, as the plucking mechanism dictates that the flexible blade experiences oscillations after one contact, and can be deviated from the equilibrium position. In this context, the voltage versus rotation speed relationship needs to be amended to reduce the possible influences of voltage fluctuation and to improve the tachometer's accuracy and linearity. Therefore, in this work we present detailed characterization of the voltage versus rotation speed relationship both theoretically and experimentally, which is the foremost step toward the precise and practical calibration criteria for self-powered triboelectric tachometers.

## 2. Model

The configuration of the low friction force triboelectric tachometer is shown in Figure 1a. To measure the rotation speed of the revolving shaft, a rigid rotor electrode is fixed onto the shaft, and a flexible stator is clamped at one end beside the shaft. This compact design eliminates the requirement of face-to-face adding, compressing and sliding the triboelectric layer with respect to the revolving surface, and is suitable for most application scenarios, especially determining the rotation speed of bearings and gears in machine tools. Moreover, the contact mechanism between rigid and flexible parts considerably reduces frictional force and wear, owing to the large deformation capability of the flexible stator. In practice, the flexible stator is clamped at a proper height to guarantee full contact area with respect to the rotor. Figure 1b shows the dynamics of the contact mechanism between the rigid and flexible parts. Suppose that the flexible stator is in the equilibrium state (both deflection and velocity equal zero), and the rigid rotor is gradually approaching from the (i) Prior to Contact state. Upon (ii) Contact state, charge pairs are generated at the interface between the polytetrafluoroethylene (PTFE) layer on the stator electrode and the rotor electrode, producing a voltage spike on external load. Thereafter is the (iii) Separation & Oscillation state, where the rigid rotor passes through and the flexible stator starts self-oscillation at its natural frequency. It is this self-oscillation process that results in the output fluctuation of the triboelectric tachometer. As the flexible stator exhibits varying deflection and velocity in the self-oscillation process, the original equilibrium state cannot be guaranteed for the next contact, and this results in change of actual deflection state and, thus, output voltage. It can be seen that the varying output voltage is deeply correlated with the self-oscillation characteristics of the flexible stator; therefore, in subsequent work we mainly investigate how the relation between natural frequency of the stator ( $f_s$ ) and the revolving frequency of the rotor ( $f$ ) affects triboelectric tachometer output. These two parameters are also presented in terms of self-oscillation cycle ( $T_s$ ) and revolving cycle ( $T$ ), as  $T_s = 1/f_s$  and  $T = 1/f$ .

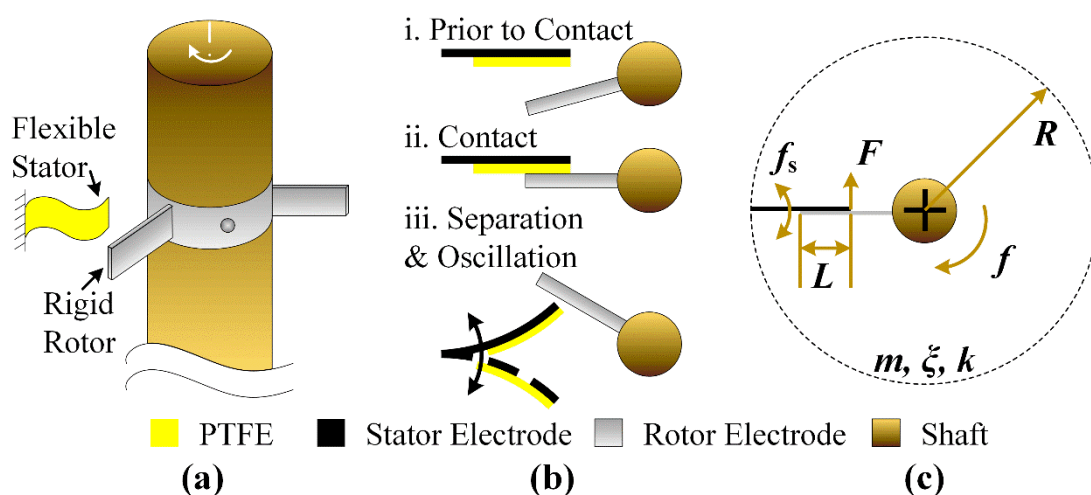


Figure 1. Triboelectric tachometer with low friction force: (a) Configuration; (b) Dynamic mechanism; (c) Model plot.

Figure 1c plots the simplified model of the triboelectric tachometer. Apart from the two key parameters  $f_s$  and  $f$  denoted above, we also adopted parameters including: mass of flexible stator ( $m$ ); spring contact of flexible stator ( $k$ ); and damping ratio ( $\zeta$ ). For ease of calculation, contact force ( $F$ ) between rigid rotor and flexible stator is assumed to be of constant value and constant duration of  $t_c$ .  $R$  and  $L$  are the geometry parameters, in which  $R$  is the radius from the revolving shaft to the flexible stator, and  $L$  is the overlapped length between rigid and flexible parts. Both  $R$  and  $L$  are assumed to be constant to guarantee constant force ( $F$ ).

The dynamics of the flexible stator is governed by Equation (1):

$$m\ddot{x} + \zeta\dot{x} + kx = \begin{cases} F & nT \leq t \leq nT + t_c \\ 0 & nT + t_c \leq t \leq (n + 1)T \end{cases} \quad (1)$$

where  $x$  is the displacement of the tip of the flexible stator, and  $n$  is arbitrary integer.

Equation (1) implicitly incorporates the key parameter  $f$  in terms of  $T$ , and the key parameter  $f_s$  in that:

$$f_s = \frac{1}{2\pi} \sqrt{\frac{k}{m}} \quad (2)$$

Based on the above two equations, the actual deflection state of the flexible stator can be described by tip displacement and velocity. Through updating the actual deflection state as the original state of Equation (1) before each contact, the dynamic characteristics of the flexible stator at different  $T$  can be derived. Based on experimentally tried and true values, we adopted specific parameters as:  $m = 0.01$  kg;  $k = 350$  N/m;  $\zeta = 0.1$ ;  $F = 1$  N; and  $t_c = 1$  ms. In this way, we set  $f_s$  to be a constant value of 29.79 Hz, i.e., the self-oscillation cycle of the flexible stator was  $T_s = 0.033$  s, but we swept the revolving cycle  $T$  to obtain varying relations between  $f_s$  and  $f$ . Figure 2 shows the calculated results of the flexible stator tip displacement and velocity at different  $T$ . The general trend shows that, when  $T \leq T_s$ , only one cycle of tip displacement or velocity change was obtained for each contact; but when  $T > T_s$ , there was more than one cycle of tip displacement or velocity change for each contact, indicating that self-oscillation was activated. For the six different  $T$  values, 100 iterations of contacts were calculated. In Figure 2, only the first 50 contacts were plotted for ease of observation. It can be seen that the transient processes completed within the first 50 contacts, and the tip displacement and velocity could maintain stability after 50 contacts. For each contact, the initial condition is marked using dots, and the maximal result is marked using diamonds. The varying dot and diamond positions in all 12 subplots demonstrate that both the initial conditions and the maximal results changed for each contact.

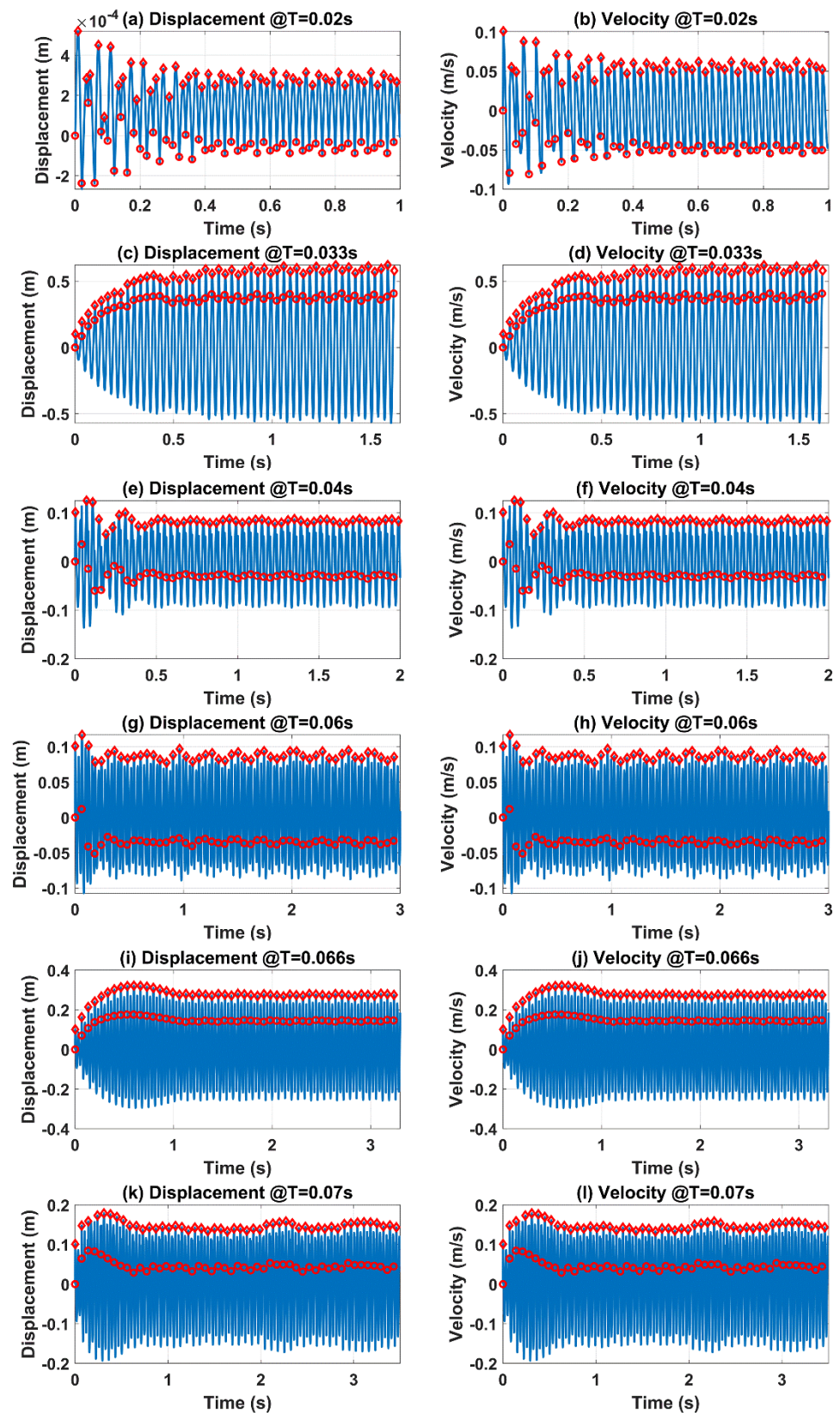


Figure 2. Calculated time traces of displacement (a,c,e,g,i,k) and velocity (b,d,f,h,j,l) at different rotation speeds.



To quantify the influence of the initial condition on tip displacement and velocity for each contact, we denoted the following two parameters:

$$\Delta d_n = d_{\max,n} - d_{0,n} \quad (3)$$

$$\Delta v_n = v_{\max,n} - v_{0,n} \quad (4)$$

where  $d_{\max,n}$  is the diamond maximal tip displacement after the  $n$ th contact, and  $d_{0,n}$  is the dotted initial tip displacement for the  $n$ th contact, so that  $\Delta d_n$  reflects maximal displacement change caused by the initial condition of the  $n$ th contact. Similarly in Equation (4),  $v_{\max,n}$  and  $v_{0,n}$  are the diamond maximal tip velocity and dotted initial tip velocity for the  $n$ th contact, and  $\Delta v_n$  reflects maximal velocity change caused by the initial condition of the  $n$ th contact.

With the help of  $\Delta d_n$  and  $\Delta v_n$ , more generalizations could be obtained from Figure 2 in terms of the maximal change of tip displacement and velocity in each contact. Taking maximal change of tip displacement as an example: in Figure 2a, when  $T = 0.02$  s,  $\Delta d_n$  first went through a transient process, and then gradually decreased to reach a stable value. Similar situations applied for  $T = 0.04$  s and  $T = 0.07$  s, as can be seen from Figure 2e,k. On the contrary, in Figure 2c, when  $T = 0.033$  s,  $\Delta d_n$  also experienced a settling process, but in an increasing trend, before finally becoming stable. Similar observations can be made for  $T = 0.06$  s and  $T = 0.066$  s, as is shown in Figure 2g,i. Maximal change of tip velocity can also be observed in similar way. Although the two generalizations can be clearly observed, it is still necessary to further quantify the decrease or increase extent of  $\Delta d_n$  and  $\Delta v_n$  for comparison, so as to obtain a clear trend of  $\Delta d_n$  and  $\Delta v_n$  versus varying  $T$  values.

To further compare  $\Delta d_n$  and  $\Delta v_n$  for different  $T$  values, normalization process is carried out as:

$$\Delta d_n^{NORM} = \frac{\Delta d_n}{\Delta d_1} \quad (5)$$

$$\Delta v_n^{NORM} = \frac{\Delta v_n}{\Delta v_1} \quad (6)$$

where  $\Delta d_1$  and  $\Delta v_1$  are the maximal displacement and velocity change caused by the initial condition of the 1st contact, i.e., caused by the equilibrium state. The normalized parameters  $\Delta d_n^{NORM}$  and  $\Delta v_n^{NORM}$  excludes the incomparable magnitude of displacement and velocity change at different  $T$  values in the form of ratios, so that they can be compared as a unit-less number versus 1, and can be characterized if the displacement and velocity change subject to current initial values outperforms or underperforms that subject to equilibrium state for one contact.

Figure 3 shows the quantified comparison of  $\Delta d_n^{NORM}$  and  $\Delta v_n^{NORM}$  for the above six different  $T$  values in all 100 contacts. In Figure 3a, all six curves of  $\Delta d_n^{NORM}$  start from the same point of  $\Delta d_1^{NORM} = 1$ , but two clear distinctions are exhibited after the settling process. For  $T = 0.033$  s, 0.06 s, and 0.066 s, all three curves of  $\Delta d_n^{NORM}$  exceeded the black dashed line of 1, while for  $T = 0.02$  s, 0.04 s, and 0.07 s, all three curves of  $\Delta d_n^{NORM}$  fell below the same dashed line of 1. This is in accordance with previous two generalizations observed in Figure 2. In addition, the normalized parameter  $\Delta d_n^{NORM}$  enables further comparison for different  $T$  values, as after stabilization  $T = 0.033$  s generated maximal  $\Delta d_n^{NORM}$  and  $T = 0.04$  s generated the minimal  $\Delta d_n^{NORM}$ . For  $T = 0.02$  s and  $T = 0.07$  s, the stable  $\Delta d_n^{NORM}$  values were very much close. Figure 3b shows the six curves of  $\Delta v_n^{NORM}$ , which are, however, quite different when compared with Figure 3a. Though all six curves still started from the same point of  $\Delta v_1^{NORM} = 1$ , all six curves exceeded the black dashed line of 1.  $T = 0.033$  s still generated maximal  $\Delta v_n^{NORM}$ , but both  $T = 0.02$  s and  $T = 0.07$  s generated the minimal  $\Delta v_n^{NORM}$ . This means that the distinction in terms of  $\Delta v_n^{NORM}$  was not as clear as that of  $\Delta d_n^{NORM}$ . Moreover, for almost all six curves of  $\Delta v_n^{NORM}$ , the deviation between contacts was much more severe compared with that of  $\Delta d_n^{NORM}$ , indicating that  $\Delta v_n^{NORM}$  is less as favorable than  $\Delta d_n^{NORM}$  in the dynamic characterization of triboelectric tachometers.

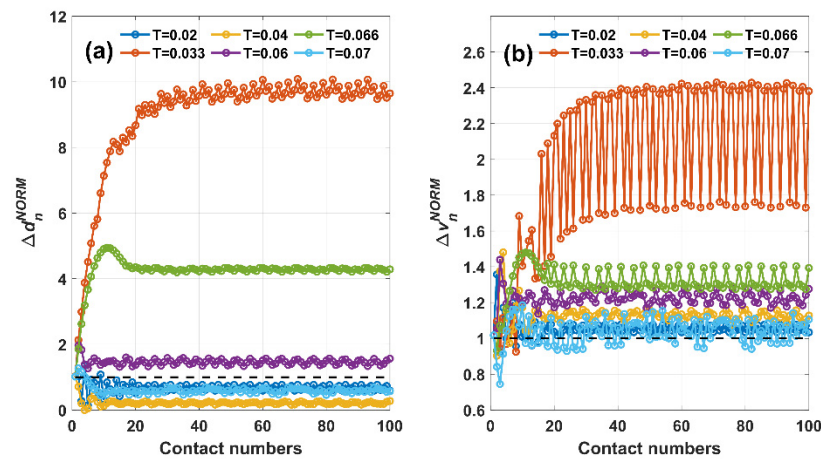


**Figure 3.** Normalized ratio vs. contact numbers: (a) displacement; (b) velocity.

In order to compare the steady state values of  $\Delta d_n^{NORM}$  and  $\Delta v_n^{NORM}$ , Figure 4 summarizes the mean and standard deviation of  $\Delta d_n^{NORM}$  and  $\Delta v_n^{NORM}$  versus varying  $T$  values. For each  $T$  value, both mean and standard deviation of  $\Delta d_n^{NORM}$  and  $\Delta v_n^{NORM}$  are calculated for the 51–100 contacts, so as to eliminate the effect of settling process. In Figure 4a, the blue curve represents mean  $\Delta d_n^{NORM}$ , and the red curve represents standard deviation of  $\Delta d_n^{NORM}$ . Interestingly, it can be seen that when  $T$  was small (i.e., comparable to stator cycle  $T_s$ ), mean  $\Delta d_n^{NORM}$  followed an oscillating style as  $T$  gradually increased, and the peaks of this oscillation decreased in this process, as is summarized in Table 1. When  $T$  was sufficiently large ( $T > 0.66$  s, i.e., cycle ratio  $T/T_s > 20$ ), such oscillation disappeared, and the mean  $\Delta d_n^{NORM}$  maintained a stable value of 1, as is plotted using the black dashed line in Figure 4a. This can be explained as follows: (1) When  $T$  is small, the influence of  $T_s$  cannot be neglected, as the flexible stator might self-oscillate to a particular deflection state other than the equilibrium state when contacts occur, and the particular deflection state changes the attainable tip displacement; (2) when  $T$  is sufficiently large, the flexible stator has sufficiently long time to recover from last contact. So, when next contact occurs, the flexible stator has resumed equilibrium state, and therefore  $\Delta d_n$  in each contact equals  $\Delta d_1$ , i.e.,  $\Delta d_n^{NORM}$  equals 1. This implies that a triboelectric tachometer can obtain accurate results for low rotation speed, but need additional calibration for high rotation speed. Additionally, the 11 highest decreasing peaks in the mean  $\Delta d_n^{NORM}$  curve have been dotted in Figure 4a and listed in Table 1. It can be seen that all these peaks occur when  $T$  is integer times of  $T_s$ , and all these peak values exceed 1. In terms of standard deviation, when  $T < 0.9$  s (i.e., cycle ratio  $T/T_s < \sim 30$ ), the standard deviation of  $\Delta d_n^{NORM}$  cannot be neglected, indicating the existence of steady state fluctuation. The maximal standard deviation of 0.4 occurred when mean  $\Delta d_n^{NORM}$  reached maximum, and for most other occasions the standard deviation was less than 0.18. When  $T > 0.9$  s, the standard deviation was zero, indicating that no steady state fluctuation existed and the triboelectric tachometer generated very stable output. Figure 4b plots the mean and standard deviation curves of  $\Delta v_n^{NORM}$  versus varying  $T$  values, and similar trend can be observed as compared to Figure 4a. When  $T$  was small, the mean  $\Delta v_n^{NORM}$  also exhibited oscillation with decreasing peaks as  $T$  gradually increased. When  $T$  was sufficiently large, the mean  $\Delta v_n^{NORM}$  also arrived at the stable value of 1 (black dashed line). However, the mean  $\Delta v_n^{NORM}$  curve contained more burrs than the mean  $\Delta d_n^{NORM}$  curve, indicating that finding the calibration criteria from the perspective of  $\Delta v_n^{NORM}$  would be more difficult and less ideal than from that of  $\Delta d_n^{NORM}$ . Still, the maximal standard deviation of 0.32 occurred when mean  $\Delta v_n^{NORM}$  reached maximum, and for most other occasions the standard deviation was approximately 0.1. Again, when  $T > 0.9$  s, the standard deviation was zero, indicating that the flexible stator was of stable velocity change. The interesting oscillation characteristics of the flexible stator shown in Figure 4 is worth further experimental validation, and following experiments mainly focus on this point.

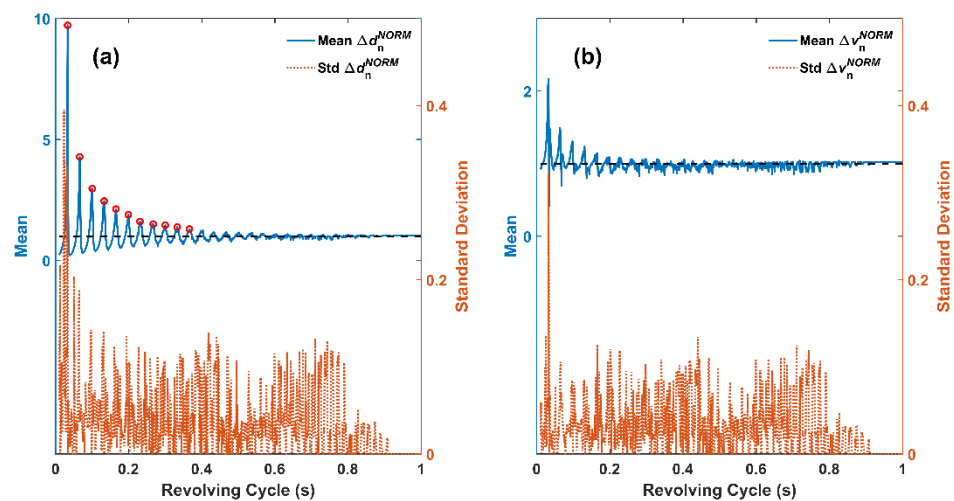


Figure 4. Mean and standard deviation of (a) displacement and (b) velocity versus revolving cycle.

Table 1. Dotted decreasing peaks in the oscillating mean  $\Delta d_n^{NORM}$  curve in Figure 4a.

Revolving Cycle $T$ (s)	Cycle Ratio $T/T_s$	Mean $\Delta d_n^{NORM}$
0.033	1.0	9.72
0.066	2.0	4.28
0.100	3.0	2.97
0.133	4.0	2.45
0.165	5.0	2.12
0.199	6.0	1.89
0.231	7.0	1.60
0.267	8.0	1.50
0.300	9.0	1.45
0.333	10.0	1.38
0.366	11.0	1.30

### 3. Experiments

Figure 5 shows the experimental setup to verify the triboelectric tachometer. For the testing rigs shown in Figure 5a, the DC motor and the circular fixtures were secured on the testing platform. The rigid rotor was fixed to the motor shaft and electrically grounded. The rotation speed of the motor was controlled by a DC voltage source (Zhaoxin MN-3205D, Shenzheng, China). The flexible stator was fastened beside the motor shaft on the circular fixtures, and the sensing signal on the flexible stator electrode was directly measured using the oscilloscope (Keysight InfiniiVision DSOX2024A, Santa Rosa, CA, USA) with 1 M $\Omega$  input resistance. Figure 5a is a snapshot in the revolution process of the motor shaft, which caused blurring of the rigid rotor and flexible stator. To show this clearly, in Figure 5b we present the close-up photo, in which the rigid rotor is connected to the motor shaft via a specialized connector, and the flexible stator bends in the contact process. The dimension of both the rigid rotor and the flexible stator was 2.95 cm  $\times$  10 cm, and the overlapped length between the rotor and the stator was 1.8 cm. Both the rotor and the stator were made of stainless steel with thicknesses of 1 mm and 0.05 mm, respectively. PTFE thin film with 90  $\mu$ m thickness (Spider (Amoy) S&T Co., Ltd., Xiamen, China) was stuck to the flexible stator, so altogether the flexible stator was 0.14 mm in thickness. For wiring, the rotor was grounded, and Figure 5c shows the measured frequency response of the flexible stator using the locked-in amplifier (Stanford Research Systems SR865, Sunnyvale, CA, USA), and the measured resonant frequency was 26.9 Hz. Inset (i) of Figure 5c is the micro-slits featured surface morphology of the PTFE film to enhance triboelectricity, and the scale bar length is 50  $\mu$ m. Inset (ii) is the finite element modal analysis of the flexible stator using ANSYS Version 14.5, and the simulated first mode resonant frequency was 28.33 Hz for the

proposed geometry, which was very close to the measured resonant frequency and the  $f_s$  value adopted in previous calculation.

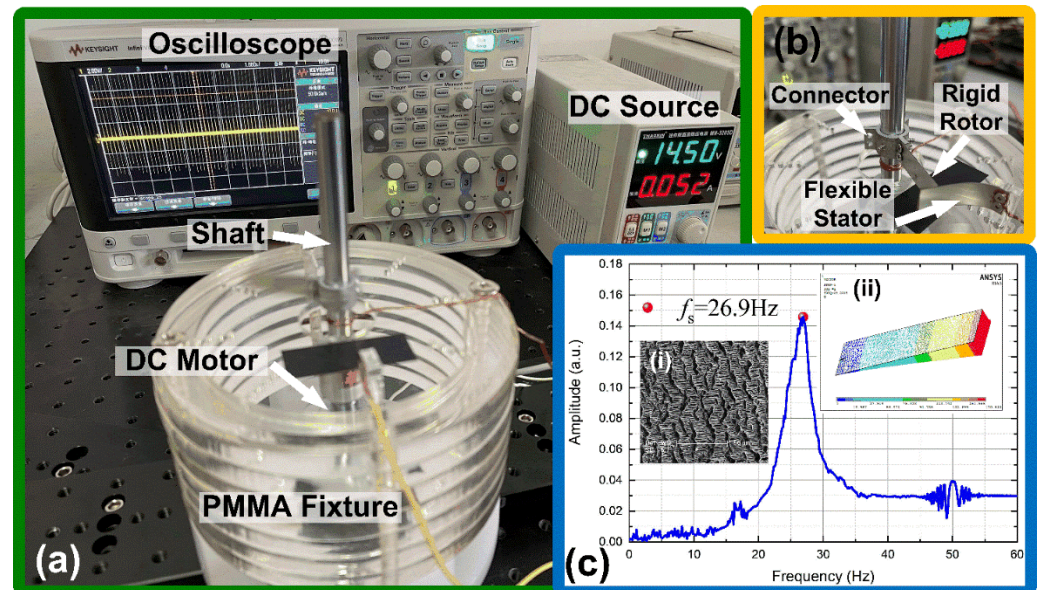


**Figure 5.** Experimental setup. (a) Photo of testing rigs; (b) Close-up photo of flexible stator and rigid rotor; (c) Frequency sweep test result of the flexible stator, showing resonant frequency of 26.9 Hz. Inset (i) in (c) is the scanning electron microscopy (SEM) photo of surface morphology of polytetrafluoroethylene (PTFE) film on the flexible stator, and Inset (ii) is the modal finite element analysis result of the flexible stator, showing theoretical resonant frequency of 28.33 Hz.

By varying the rotation speed of the motor shaft, the sensing signals on the stator electrode were measured and shown in Figure 6. Altogether we measured 43 different rotation speeds spanning from 45 revolutions per minute (rpm) to 560 rpm, as these two values were the experimentally attainable lowest and highest rotation speeds of our DC motor. In Figure 6, 8 of the 43 different rotation speeds are picked out as an illustration, namely 135 rpm, 170 rpm, 230 rpm, 365 rpm, 425 rpm, 475 rpm, 515 rpm, and 560 rpm. The corresponding revolving frequency for these 8 rotation speeds was 2.25 Hz, 2.83 Hz, 3.83 Hz, 6.08 Hz, 7.08 Hz, 7.92 Hz, 8.58 Hz, and 9.33 Hz, and the respective revolving cycle decreased from 0.44 s, 0.35 s, 0.26 s, 0.16 s, 0.14 s, 0.13 s, 0.12 s, to 0.11 s. At all rotation speeds, the triboelectric voltage-time curves were recorded, and the general trend was a series of voltage spikes corresponding to a series of contacts. In this work, the peak-to-peak voltage ( $V_{pp}$ ) of these voltage spikes was adopted to characterize the triboelectric tachometer output, so as to avoid the possible positive and negative voltage asymmetry and to better reflect the total triboelectric output voltage generated at different rotation speeds. In all subplots of Figure 6, the maximal positive triboelectric voltage for all contacts is marked using dots, and the minimal negative triboelectric voltage is marked using diamonds.  $V_{pp}$  for each contact was calculated as the difference between the maximal and minimal voltage value, and the measured multiple  $V_{pp}$  values were averaged over the same testing period of 10 s for each rotation speed. Throughout the subplots, it can be seen that the averaged  $V_{pp}$  values were 1.16 V, 2.25 V, 8.59 V, 7.88 V, 4.50 V, 18.37 V, 5.19 V, and 17.87 V for the above rotation speeds, demonstrating that no simple linear relationship existed for generated voltage and rotation speed. Rather, the generated voltage also exhibits in an oscillating fashion as the rotation speed increases.



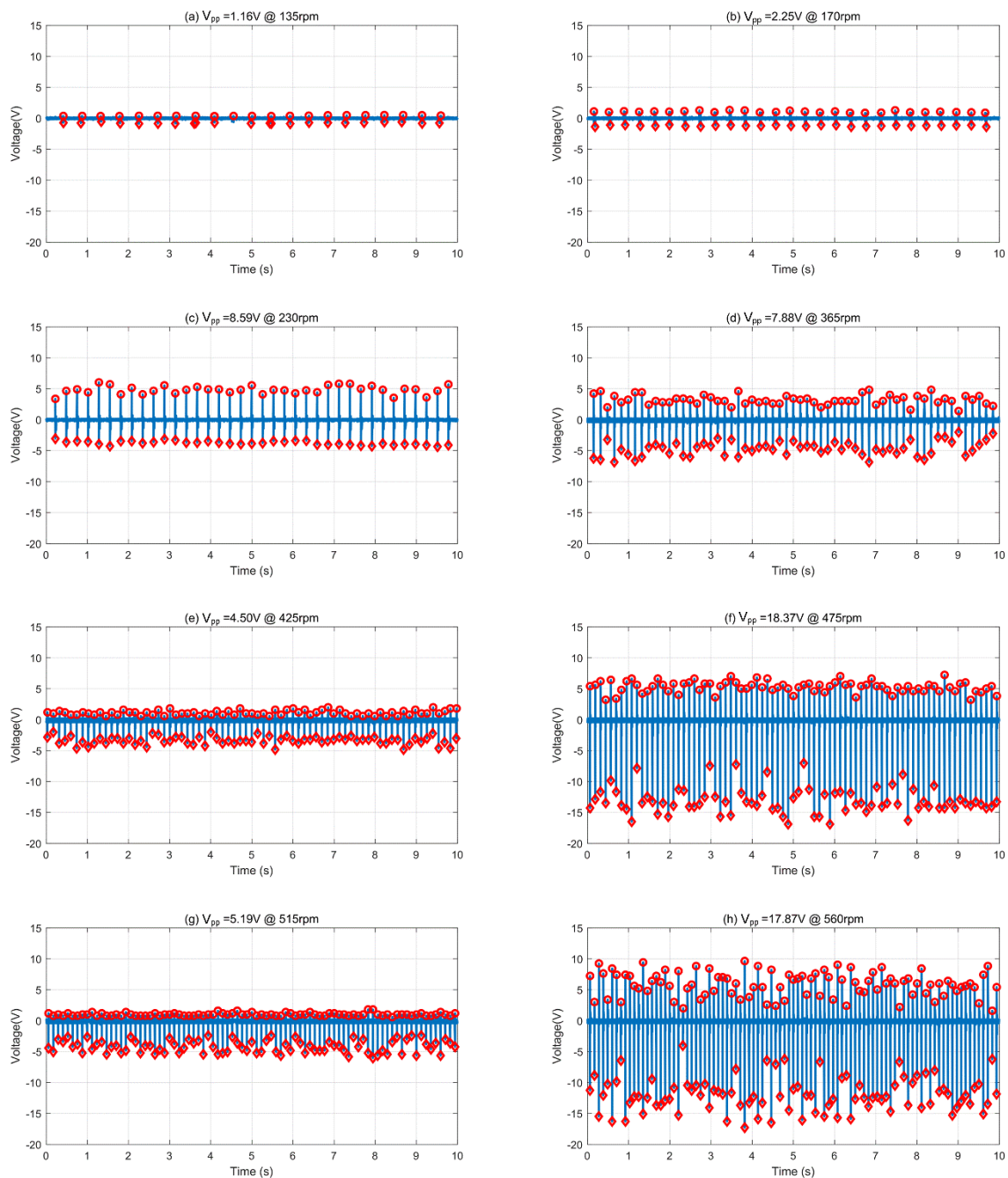


**Figure 6.** Measured voltage–time curves at different rotation speeds.

To better clarify the relation between the triboelectric voltage of the tachometer and rotation speed, Figure 7 further plots the relation of voltage ratio versus cycle ratio based on five sets of voltage data measured for all 43 rotation speeds. In Figure 7, the vertical axis of voltage ratio is defined as the ratio of voltage at specific rotation speed over voltage at 45 rpm. In other words, because 45 rpm represents a relatively long revolving cycle for the flexible stator to resume its equilibrium state, this voltage ratio can also be understood as the normalized voltage with respect to the equilibrium state. The horizontal axis of cycle ratio is defined as the ratio of rotor revolving cycle  $T$  over stator self-oscillation cycle  $T_s$ , or the reciprocal of rotor revolving frequency  $1/f$  multiplied by stator resonant frequency  $f_s$ . In other words, this cycle ratio equals  $T/T_s$  or  $f_s/f$ . For all 43 datapoints averaged over five sets, the voltage ratio showed an oscillating style with respect to the cycle ratio. In Figure 7, all crests in the 43 datapoints are marked using pentagons, and all troughs are

marked using squares. Both the crests and the troughs can be fitted exponentially, and these two exponentially fitted lines constitute the upper and lower limit of the experimental datapoints. For the tachometer function, the oscillating part of the curve in Figure 7 (i.e., cycle ratio is less than 15) could serve as the calibration criteria for measuring and characterizing rotation speed of the motor shaft. When the revolving cycle to be measured was sufficiently large, i.e., cycle ratio is greater than 15, the oscillation feature disappeared as both crests and troughs coincided with the datapoints. In this condition, the voltage ratio and cycle ratio curve could be degraded into a unified exponential curve. Apart from the voltage characterization method, the inset (i) in Figure 7 shows an alternative method of measuring the rotation speed via averaging the timespan between triboelectric voltage spikes, which also shows good sensitivity and linearity. The slope of curve between measured rotation speed and set rotation speed was 0.9939, which is very close to 1.

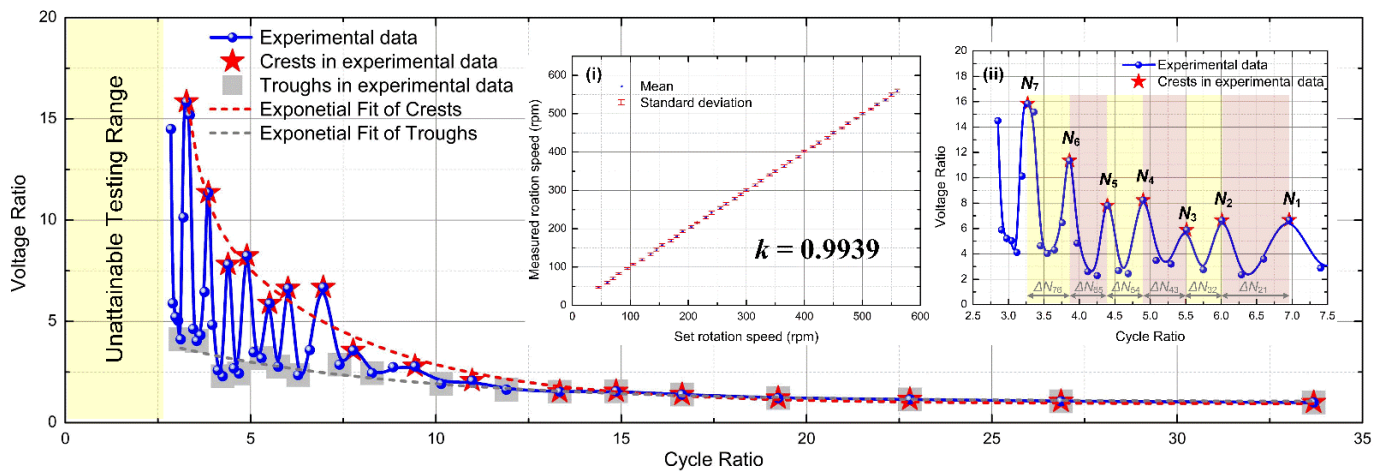


**Figure 7.** Characterization of measured voltage ratio vs. cycle ratio, with inset (i) sensitivity of the triboelectric tachometer based on time measurement of voltage spikes; (ii) close-up of the voltage ratio oscillation in the range of 2.5–7.5 cycle ratio.

Inset (ii) in Figure 7 shows the close-up of the highest seven crests, which are marked as  $N_1$  to  $N_7$  from right to left. This close-up shows the oscillating style with decreasing peaks more clearly. However, further characterization of the distance between these seven crests indicated a slight deviation from the theoretical model. The distance between adjacent crests  $\Delta N_{ij}$  is defined as:

$$\Delta N_{ij} = \Delta N_j - \Delta N_i \quad i > j \in [1, 2, \dots, 7] \quad (7)$$

and the results of the six  $\Delta N_{ij}$  are shown in Table 2. It can be seen that the distances between the peaks actually decreased as cycle ratio reduced, and the peaks did not necessarily occur at integer times of the stator self-oscillation cycle  $T_s$  as shown in Table 1. This deviation is possibly due to the discrepancy with previous model assumption, as the duration of contact force  $F$  between rigid rotor and flexible stator may also have fluctuated. Future works can concentrate on this point to present a more detailed specification of the oscillating feature of the triboelectric tachometer proved in this paper, which will further refine the sensor calibration and shed more light on potential self-powered sensing applications.

**Table 2.** Distance between highest seven crests in terms of cycle ratio.

$\Delta N_{21}$	$\Delta N_{32}$	$\Delta N_{43}$	$\Delta N_{54}$	$\Delta N_{65}$	$\Delta N_{76}$
0.94	0.60	0.62	0.60	0.53	0.50

#### 4. Conclusions

An alternative self-powered triboelectric tachometer with low friction force is presented in this study, which in structure contained a rigid rotor and flexible stator, and in principle utilized the flapping between triboelectric layers on both rigid and flexible parts. The model of this device has been analytically solved, and results show that both the displacement and velocity of the flexible stator tip followed an oscillating style with decreasing peaks as rotation cycle increased, among which tip displacement exhibited a more consistent trend with less fluctuation and deviation. Experimentally, the proposed device was adopted for rotation speed measurement, and the oscillating curve of output voltage versus rotation speed was verified. For the proposed device, the slope of measured rotation speed vs. set rotation speed was 0.9939, demonstrating high linearity. In the future, the proved oscillating relationship could be further refined in terms of contact force duration, and could potentially be applied as calibration criteria for further improving the sensitivity and linearity of triboelectric tachometers.

**Author Contributions:** Conceptualization, L.B.; methodology, L.B. and X.H.; software, F.L.; validation, X.H., L.Q., Z.W. and F.Z.; formal analysis, X.H., L.Q., Z.W. and F.Z.; investigation, X.H.; data curation, F.L.; writing—original draft preparation, L.B.; writing—review and editing, T.L.; visualization, T.L.; supervision, L.B.; project administration, L.B.; funding acquisition, L.B. All authors have read and agreed to the published version of the manuscript.

**Funding:** This research was funded by National Natural Science Foundation of China, grant number 61834003.

**Conflicts of Interest:** The authors declare no conflict of interest.

#### References

1. Chae, H.; Park, G.; Lee, J.; Kim, K.; Kim, T.; Kim, H.S.; Seo, T.T. Façade cleaning robot with manipulating and sensing devices equipped on a gondola. *IEEE/ASME Trans. Mech.* **2021**, *26*, 1719–1727. [[CrossRef](#)]
2. Gao, Q.; Cheng, T.H.; Wang, Z.L. Triboelectric mechanical sensors—Progress and prospects. *Extrem. Mech. Lett.* **2021**, *42*, 101100. [[CrossRef](#)]
3. Yang, X.; Chen, S.; Shi, Y.; Fu, Z.; Zhou, B. A flexible highly sensitive capacitive pressure sensor. *Sens. Actuators A-Phys.* **2021**, *324*, 112629. [[CrossRef](#)]
4. Bai, P.; Zhu, G.; Liu, Y.; Chen, J.; Jing, Q.; Yang, W.; Ma, J.; Zhang, G.; Wang, Z.L. Cylindrical rotating triboelectric nanogenerator. *ACS Nano* **2021**, *7*, 6361–6366. [[CrossRef](#)]
5. Kim, T.; Chung, J.; Kim, D.Y.; Moon, J.H.; Lee, S.; Cho, M.; Lee, S.H.; Lee, S. Design and optimization of rotating triboelectric nanogenerator by water electrification and inertia. *Nano Energy* **2016**, *27*, 340–351. [[CrossRef](#)]
6. Zhou, Q.; Chen, S.; Lai, J.; Deng, S.; Pan, J.; Baibk, J.M.; Xia, F. High rotational speed hand-powered triboelectric nanogenerator toward a battery-free point-of-care detection system. *RSC Adv.* **2021**, *11*, 23221–23227. [[CrossRef](#)]
7. Liu, Y.; Zhao, W.; Liu, G.; Bu, T.; Xia, Y.; Xu, S.; Zhang, C.; Zhang, H. Self-powered artificial joint wear debris sensor based on triboelectric nanogenerator. *Nano Energy* **2021**, *85*, 105967. [[CrossRef](#)]
8. Lu, S.; Gao, L.; Chen, X.; Tong, D.; Lei, W.; Yuan, P.; Mu, X.; Yu, H. Simultaneous energy harvesting and signal sensing from a single triboelectric nanogenerator for intelligent self-powered wireless sensing systems. *Nano Energy* **2020**, *75*, 104813. [[CrossRef](#)]
9. Long, S.; Feng, Y.; He, F.; Zhao, J.; Bai, T.; Lin, H.; Cai, W.; Mao, C.; Chen, Y.; Gan, L.; et al. Biomass-derived, multifunctional and wave-layered carbon aerogels toward wearable pressure sensors, supercapacitors and triboelectric nanogenerators. *Nano Energy* **2021**, *85*, 105973. [[CrossRef](#)]
10. Li, R.; Wei, X.; Xu, J.; Chen, J.; Li, B.; Wu, Z.; Wang, Z.L. Smart wearable sensors based on triboelectric nanogenerator for personal healthcare monitoring. *Micromachines* **2021**, *12*, 352. [[CrossRef](#)] [[PubMed](#)]
11. Zhang, W.; Zhang, Y.; Yang, G.; Hao, X.; Lv, X.; Wu, F.; Liu, J.; Zhang, Y. Wearable and self-powered sensors made by triboelectric nanogenerators assembled from antibacterial bromobutyl rubber. *Nano Energy* **2021**, *82*, 105769. [[CrossRef](#)]
12. Chen, G.; Xu, L.; Zhang, P.; Chen, B.; Wang, G.; Ji, J.; Pu, X.; Wang, Z.L. Seawater degradable triboelectric nanogenerators for blue energy. *Adv. Mater. Technol.* **2020**, *5*, 1–8. [[CrossRef](#)]
13. Jiang, T.; Pang, H.; An, J.; Lu, P.; Feng, Y.; Liang, X.; Zhong, W.; Wang, Z.L. Robust swing-structured triboelectric nanogenerator for efficient blue energy harvesting. *Adv. Energy Mater.* **2020**, *10*, 1–9. [[CrossRef](#)]
14. Wang, Z.L.; Jiang, T.; Xu, L. Toward the blue energy dream by triboelectric nanogenerator networks. *Nano Energy* **2017**, *39*, 9–23. [[CrossRef](#)]

15. Zhong, Y.; Guo, Y.; Wei, X.; Rui, P.; Du, H.; Wang, P. Multi-cylinder-based hybridized electromagnetic-triboelectric nanogenerator harvesting multiple fluid energy for self-powered pipeline leakage monitoring and anticorrosion protection. *Nano Energy* **2021**, *89*, 106467. [[CrossRef](#)]
16. Wang, Y.; Wu, C.; Yang, S. A self-powered rotating speed sensor for downhole motor based on triboelectric nanogenerator. *IEEE Sens. J.* **2021**, *21*, 4310–4316. [[CrossRef](#)]
17. Soin, N.; Fishlock, S.J.; Kelsey, C.; Smith, S. Triboelectric effect enabled self-powered, point-of-care diagnostics: Opportunities for developing assured and reassured devices. *Micromachines* **2021**, *12*, 337. [[CrossRef](#)]
18. Li, W.; Zhou, J. Novel laser Doppler tachometer. *Chin. Opt. Lett.* **2021**, *19*, 28–34. [[CrossRef](#)]
19. Gao, S.; Su, J.; Wei, X.; Wang, M.; Tian, M.; Jiang, T.; Wang, Z.L. Self-powered electrochemical oxidation of 4-aminoazobenzene driven by a triboelectric nanogenerator. *ACS Nano* **2017**, *11*, 770–778. [[CrossRef](#)]
20. Roh, H.; Yu, J.; Kim, I.; Chae, Y.; Kim, D. Dynamic analysis to enhance the performance of a rotating-disk-based triboelectric nanogenerator by injected gas. *ACS Appl. Mater. Inter.* **2019**, *11*, 25170–25178. [[CrossRef](#)] [[PubMed](#)]
21. Yun, J.; Roh, H.; Choi, J.; Gu, D.; Kim, D. Disk triboelectric nanogenerator-based nonvolatile memory toward smart identification system. *Adv. Funct. Mater.* **2021**, *31*, 1–11. [[CrossRef](#)]
22. Tcho, I.W.; Jeon, S.B.; Park, S.J.; Kim, W.G.; Jin, I.K.; Han, J.k.; Kim, D.; Choi, Y.K. Disk-based triboelectric nanogenerator operated by rotational force converted from linear force by a gear system. *Nano Energy* **2018**, *50*, 489–496. [[CrossRef](#)]
23. Choi, Y.; Hong, D.; Choe, J.; Lee, Y.; Jeong, J. Test bed for rotation-based triboelectric nanogenerators. *Rev. Sci. Instrum.* **2020**, *91*, 036101.
24. Bai, Y.; Xu, L.; Lin, S.; Luo, J.; Qin, H.; Han, K.; Wang, Z.L. Charge pumping strategy for rotation and sliding type triboelectric nanogenerators. *Adv. Energy Mater.* **2020**, *10*, 1–9. [[CrossRef](#)]
25. Xie, Y.N.; Wang, S.H.; Niu, S.M.; Lin, L.; Jing, Q.S.; Su, Y.J.; Wu, Z.Y.; Wang, Z.L. Multi-layered disk triboelectric nanogenerator for harvesting hydropower. *Nano Energy* **2014**, *6*, 129–136. [[CrossRef](#)]
26. Wang, P.; Pan, L.; Wang, J.; Xu, M.; Dai, G.; Zou, H.; Dong, K.; Wang, Z.L. An ultra-low-friction triboelectric-electromagnetic hybrid nanogenerator for rotation energy harvesting and self-powered wind speed sensor. *ACS Nano* **2018**, *12*, 9433–9440. [[CrossRef](#)] [[PubMed](#)]
27. Zhang, N.; Qin, C.; Feng, T.; Li, J.; Yang, Z.; Sun, X.; Liang, E.; Mao, Y.; Wang, X. Non-contact cylindrical rotating triboelectric nanogenerator for harvesting kinetic energy from hydraulics. *Nano Res.* **2020**, *13*, 1903–1907. [[CrossRef](#)]
28. Wu, C.; Fan, C.; Wen, G. Self-powered speed sensor for turbodrills based on triboelectric nanogenerator. *Sensors* **2019**, *19*, 4889. [[CrossRef](#)] [[PubMed](#)]
29. Lin, Z.; Zhang, B.; Zou, H.; Wu, Z.; Guo, H.Y.; Zhang, Y.; Yang, J.; Wang, Z.L. Rationally designed rotation triboelectric nanogenerators with much extended lifetime and durability. *Nano Energy* **2020**, *68*, 104378. [[CrossRef](#)]
30. Bu, L.; Chen, Z.; Chen, Z.; Qin, L.; Yang, F.; Xu, K.; Han, J.; Wang, X.H. Impact induced compound method for triboelectric-piezoelectric hybrid nanogenerators to achieve Watt level average power in low frequency rotations. *Nano Energy* **2020**, *70*, 104500. [[CrossRef](#)]